Crosstalk-mitigated microelectronic control for optically active spins

Hao-Cheng Weng,* John G. Rarity, and Krishna C. Balram
Quantum Engineering Technology Labs, H. H. Wills Physics Laboratory and Department of Electrical and Electronic Engineering, University of Bristol, Bristol BS8 1TL, United Kingdom

Joe A. Smith†
School of Electrical and Electronic Engineering, University of Sheffield, Sheffield S1 3JD, United Kingdom and Quantum Engineering Technology Labs, H. H. Wills Physics Laboratory and Department of Electrical and Electronic Engineering, University of Bristol, Bristol BS8 1TL, United Kingdom

(Received 12 July 2025; revised 1 November 2025; accepted 23 December 2025; published 9 February 2026)

To exploit the subnanometer dimensions of qubits for large-scale quantum information processing, corresponding control architectures require both energy and space efficiency, with the on-chip footprint of unit-cell electronics ideally being micrometer scale; however, the spin coherence of qubits in close packing is severely deteriorated by microwave crosstalk from neighboring control sites. Here, we present a crosstalk-mitigation scheme using foundry microelectronics to address solid-state spins at sub-100-μm spacing without the need for qubit detuning. Using nitrogen-vacancy centers in nanodiamonds as qubit prototypes, we first demonstrate 10-MHz Rabi oscillations at milliwatt-level microwave power. By implementing active cancellation, we then demonstrate that the crosstalk field from neighboring lattice sites can be reduced to undetectable levels. We finally extend the scheme to show increased qubit control, or, effectively, enhanced spin coherence under crosstalk mitigation. Compatible with integrated optics, our results present a step toward scalable control across quantum platforms using silicon microelectronics.

DOI: 10.1103/stgn-ysxr

I. INTRODUCTION

The field of quantum computing, underscored by demonstrations of computational quantum advantage [1,2], has shifted toward engineering scalable systems, both in terms of qubit quality (coherent gate operations [3]) and quantity ($>10^6$ qubits) [4,5].

To scale up, the key advantage of solid-state systems is the prospect of achieving close packing of qubits, taking into account energy efficiency and space constraints in cryogenic operations; however, for large-scale systems, performance becomes limited by classical control and wiring [6,7], especially when close packing brings with it the problem of qubit crosstalk between neighboring controls. Without microwave-crosstalk mitigation, two identical qubits must be separated by millimeters, which prohibits placing more than a few qubits on the same chip (5×5 mm^2) and prevents scalability in any meaningful sense.

A variety of control signals for quantum systems fall into the megahertz to gigahertz-frequency domain [8,9]. These systems range from superconducting transmon qubits to spin qubits in solid-state systems and trapped ions [10–12], where two-level systems are addressed by microwave pulses. Progress on crosstalk mitigation has been made, particularly in superconducting qubits [13]; however, these designs are not directly adaptable to qubits with optical access, such as color centers in diamond, 2D materials, and trapped ions. Close proximity of metallic structures to optics enhances scattering and photon loss, posing a significant challenge.

Previous works on trapped ions [14] have employed gradient fields to provide unique frequency addressability to each qubit, preventing crosstalk. For solid-state defects, recent works have proposed alternative spin-driving schemes with strain-tunable electrodes [15] and electromechanical control [16] to achieve localized control fields. Nevertheless, requiring distinct microwave frequencies per qubit is experimentally costly, and mechanical control is challenging to fabricate.

In this work, we present a design for site-defined control using silicon microelectronics, prototyping with foundry application-specific integrated circuits (ASICs)

*Contact author: haocheng.weng@bristol.ac.uk
†Contact author: joe.a.smith@sheffield.ac.uk

Published by the American Physical Society under the terms of the Creative Commons Attribution 4.0 International license. Further distribution of this work must maintain attribution to the author(s) and the published article's title, journal citation, and DOI.

and nitrogen-vacancy (NV) centers in diamond. NVs are well characterized spin qubits with optical interfaces [17–19]. Moreover, the room-temperature operation of NV spin systems and their pointlike localization make them ideal prototypes for testing large-scale control architectures in the gigahertz regime.

The complexity of microelectronics allows fabricable quantum control systems at submillimeter scale [20], as compared to the macroscale metallization typically realized with printed circuit boards [21]. We introduce a dual-loop transducer ASIC design that effectively isolates single control sites at sub-100-μm qubit packing densities. Our results illustrate the possibility of scalable control for spins individually and simultaneously in a compact device. The scheme is scalable and paves the way for further combination with active microelectronics and integrated optics.

II. ACTIVE CROSSTALK CANCELLATION

Spin-based quantum systems are commonly electrically driven by a close metallic structure to ensure efficient and localized manipulation; however, for optically active spins, this structure should be located several optical wavelengths away from the spin to prevent optical scattering and a decrease in photonic efficiency. Therefore, there is a trade-off between the deliverable localized field at the spin and the need to reduce optical loss by keeping the metallic structure at some distance from the dipole-like emission. To account for this, we introduce a square loop geometry [in Fig. 1(a)] for dedicated spin control of each site. This maximizes the area into which photonic structures can be introduced while also maximizing the contact area of the driving transducer for a concentrated and directed field.

As microwave controls for spin systems have a near infinite wavelength $\lambda > 1$ cm, compared to micrometer

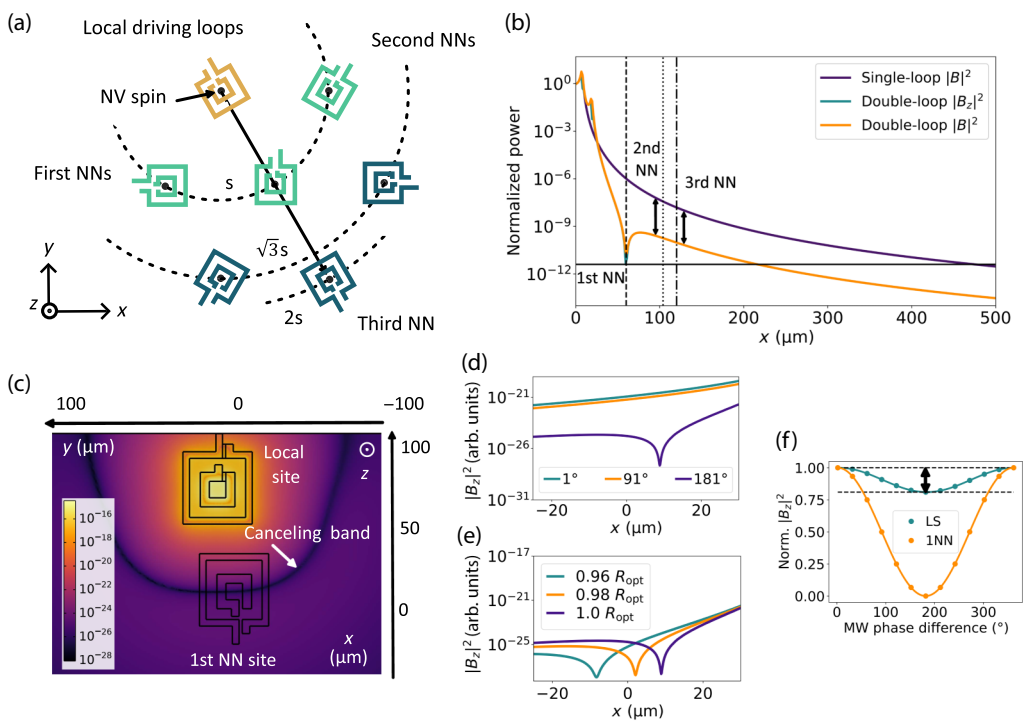

FIG. 1. Active crosstalk-cancelation scheme. (a) Hexagonal packing of driving sites: for the upper-left (golden) site, the sites in light green are first nearest-neighbor (NN) sites at a distance of s. The second NN sites (in dark green) and third NN sites (in purple) are $\sqrt{3}s$ and $2s$ away, respectively. Each site is represented by two concentric loops hosting a spin qubit (black dot in the center) set in the x-y plane, where the outer loop produces a canceling signal out of phase with the inner loop signal. (b) Comparison of the magnetic field power at different distances from the local driving site, showing field cancelation (see the analytical simulation method in Appendix A). The power attenuation at second and third NN sites is indicated. (c) Results of a finite-element simulation of this structure conducted following foundry-microelectronics design rules. The outer loops are 38 μm in diameter and the inner loops are 15.5 μm in diameter. The power of the out-of-plane magnetic field component $|B_z|^2$ is plotted. The plot of magnetic field power has units of tesla squared when driven at 1 V by a 50-ω coaxial source. The same unit applies for (d) and (e). (d) The field cancelation is shown precisely when the phase difference (lines in graph) is 181° in the simulation. (e) The point of maximal cancelation is spatially tuned by changing the driving ratio R_{opt} between the two loops. (f) Comparison of the driving power $|B_z|^2$ at the local site (LS) and the first NN site (1NN), in a sweep of the set microwave phase difference between the inner and outer loop.

features, their spatial extent can be significant, deleteriously affecting secondary systems located nearby. For a single loop delivering 0 dB power to the control site at the origin, a significant power (−60 dB or a 0.5% reduction of the spin coherence time; see Appendix A) remains at 60 μm from the center [purple line in Fig. 1(b)]. Common methods to remove the residual field, such as enclosing Faraday cages or lead shielding, are incompatible with planar fabrication processes. Resonators with much smaller mode volumes are also challenging, with precise impedance matching becoming unreliable on micrometer-scale devices [22], along with the aforementioned requirements of optical access.

Nonetheless, by adopting multilayer metallization from silicon microelectronics, we gain the flexibility to route signals out of the plane, enabling complex geometries. In this work, we exploit this by using two lithographically defined concentric loops, as shown in Fig. 1(a). By driving the two loops 180° out of phase, the counterpropagating fields cancel away from the local control site. With finite-width current-carrying wires and a rectangular geometry, we examine the cancelation in a fabricable device through a gigahertz finite-element simulation (Appendix B). Note that the square shape of the loops is constrained by foundry design rules for the metal layer and behaves similarly to circular loops (Appendix A). In Fig. 1(c), we show the magnetic field power ($|B_z|^2$) for this device containing a local driving site and a first NN site. By setting the driving current ratio and phase difference, the maximally canceled region forms a band of 350 nm width (as defined by the spatial tolerance; see [23] for details). In Fig. 1(d), by tuning the relative phase between the feeds driving each loop, complete cancelation occurs at 181°, producing −50 dB attenuation at the first NN [$x = 10$ μm following the coordinates in Fig. 1(c)]. The canceling point can be fine tuned spatially by changing the driving ratio between the two loops. In Fig. 1(e), by sweeping the driving voltage ratio R between the inner and outer loops at the local site around R_{opt}, the optimized ratio such that cancelation occurs at $x = 10$ μm, the dip can be tuned between $x = 0$ and 20 μm. In Fig. 1(f), we compare the field at the local site center [top of Fig. 1(c)] and the remote site (bottom). Along the phase sweep, only a slight reduction in power (<20%) is observed at the local site. This allows the canceling scheme to operate without significantly sacrificing the local driving field. In practice, once the cancelation condition is found, the microwave source amplitude can be scaled to achieve the desired driving power.

This design allows (i) a much more localized field and (ii) precise cancelation of the field at a distance corresponding to the first NN sites. To see how the two-loop scheme works, we compare the total magnetic power $|B|^2$ (normalized to the control site at $x = 0$) at NN sites spaced with hexagonal packing [Fig. 1(b), orange line]. The field cancels perfectly at the first NN site ($x = 60$ μm), showing high power suppression (−120 dB, when 0 dB is delivered at $x = 0$), or equivalently an additional −50 dB attenuation compared to the single-loop case. As the dominant field component is in the z direction, the two-loop $|B|^2$ extinction ratio is similar to that of $|B_z|^2$. At the second and third NN sites ($x = 104$ and 120 μm), as the field decays faster in the two-loop scheme (following a $1/x^{15}$ power-law decay as compared to the $1/x^6$ decay for the single-loop scheme when fitted), an additional −20 dB power attenuation is applied. The scheme scales for all NN sites at the same distance from the local site.

III. HYBRID DEVICE REALIZATION

To demonstrate the active crosstalk cancelation in a scalable platform, we leverage a commercial 0.13 μm back-end-of-line silicon foundry process with aluminium layers, isolated with silicon dioxide, and tungsten vias (see Appendix D). Unlike printed circuit boards (PCBs), a millimeter-scale technology that is constrained by the use of plated holes to form through-plane vias, a silicon foundry process allows us to achieve micrometer-scale features. In Fig. 2(a), the structure is realized in two rectangular loops of the same dimensions, following the gigahertz finite-element simulation results in Figs. 1(c)–1(f). As a demonstration, nanodiamonds containing single optically accessible NVs are lithographically positioned in a post-processing step (see Appendix C). The structure imaged using scanning electron microscopy is shown in Fig. 2(b). The hybrid device is studied with confocal microscopy

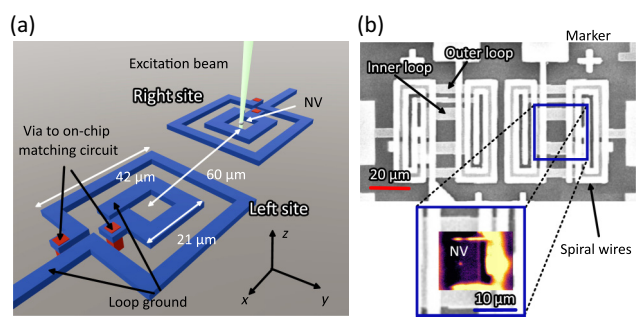

FIG. 2. Hybrid microelectronic device. (a) Schematic of the hybrid device showing the dual-loop structures realized on an ASIC, combined with an NV center in a nanodiamond. The dimensions of the inner and outer loops follow those simulated in Fig. 1(c). The right-hand site shows the NV in the positioned nanodiamond addressed by the excitation laser (see details in Appendix C). One end of each loop is connected to ground and the other is connected to the on-chip matching circuit through the red vias (see Appendix C). (b) An exemplar scanning electron microscope image of the device. Markers are used during the positioning process for alignment. The loop structures are underneath spiral wires not used in the current experiment. The inset shows a confocal scan of the optically active NV (shown by the central Gaussian spot) in the center of the structure.

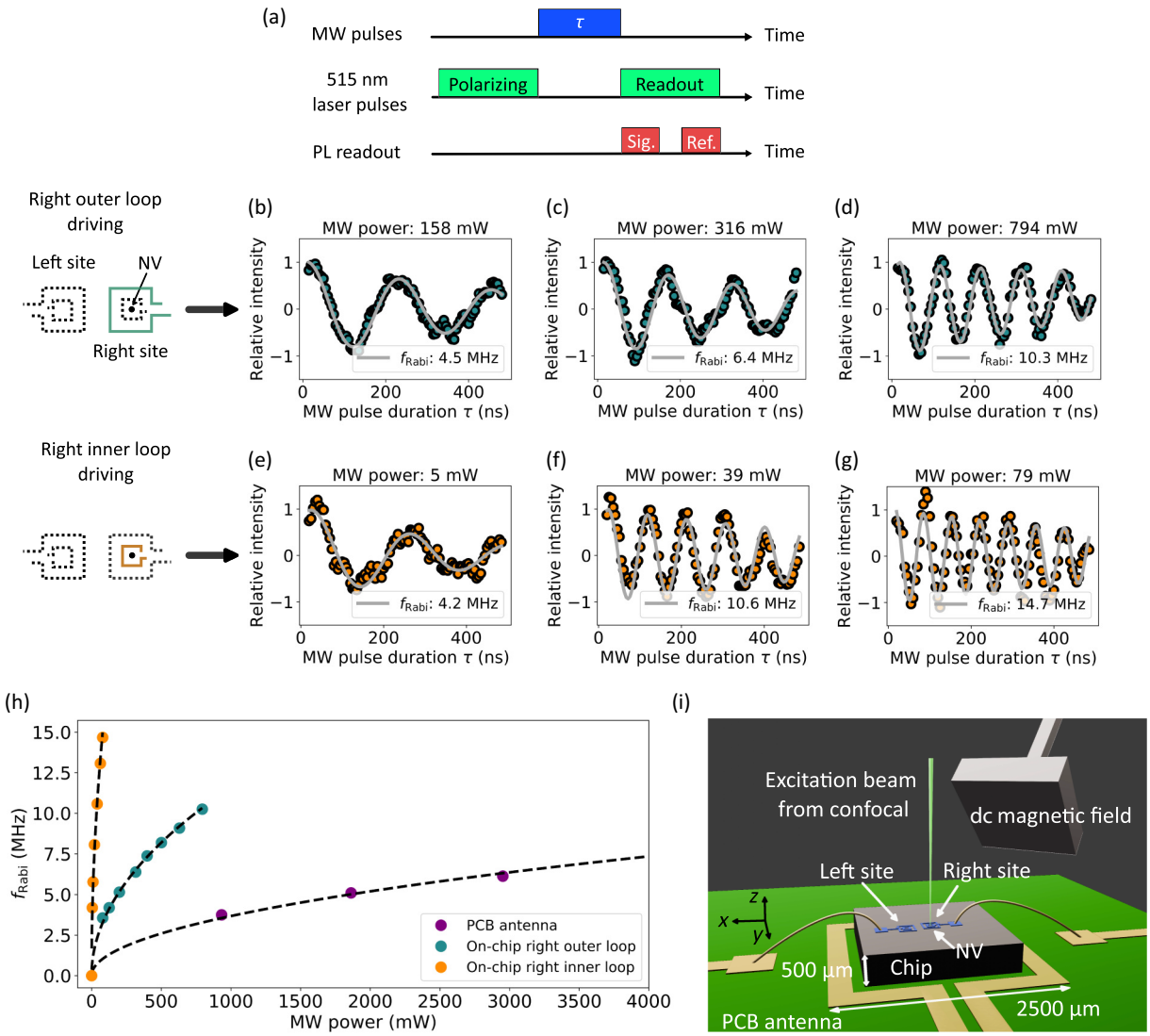

FIG. 3. On-chip electron spin driving. (a) Pulse sequences for Rabi oscillation experiments. The first part of the photoluminescence (PL) readout is the signal (Sig.) that contributes to the state-dependent intensity contrast, and the second part is a reference (Ref.) for normalization of counts. The metallic loops are studied by performing Rabi oscillations on the same NV electron spin. The spin associated with the isolated NV is driven by the on-chip right-hand outer loop [(b)–(d) in green] and the on-chip right-hand inner loop [(e)–(g) in orange] showing the Rabi oscillation at different driving microwave (MW) power levels. Note that where the geometry is shown by a dashed line, this indicates that the structure is not driven. The applied microwave power and Rabi frequency are labeled. Here, the microwave power is normalized to the loop S_{11} efficiency, i.e., the microwave reflection coefficient (see Appendix D), representing the power delivered by the loop structures. (h) Comparing the on-chip loop structures to the global PCB antenna demonstrates an observed 200-fold improvement in driving efficiency above 10 MHz. (i) Schematic diagram showing the spatial relations between the on-chip loops and the PCB antenna. Dimensions are not to scale.

under 515-nm laser excitation to identify an isolated NV at the control site [Fig. 2(b), inset] through photoluminescence (PL).

The on-chip loops (with on-chip matching circuitry; see Appendix C) are then connected to external electronics and microwave sources (see Appendix D). By controlling the NV in Fig. 2(b), we can evaluate the microelectronics performance for manipulating a quantum system. We perform Rabi oscillations on the NV electron spin (see Appendix D) by applying microwave and laser pulses presented in Fig. 3(a). As the microwave pulse width τ is swept, the oscillation of PL intensity reveals the spin-state transition at a frequency f_{Rabi} proportional to the square root of the applied microwave power. We compare the Rabi oscillation of the same enclosed NV when driven with the on-chip right-hand outer loops [Figs. 3(b)–3(d)] and right-hand inner loops [Figs. 3(e)–3(g)], following the labels in Fig. 2(a).

In Fig. 3(h), plotting the power dependence of the observed Rabi frequency indicates that on-chip driving (compared to driving with the global PCB antenna; see Appendix D) is significantly more efficient, as expected from the micrometer proximity to the radiation source (following the $1/r^3$ power-law decay, where r is the distance from the source), as opposed to approximately 500 μm for the external antenna [Fig. 3(i)]. The inner loop also drives more efficiently than the outer loop. Specifically, our result shows that the on-chip metallic loop interface can be 200 times more efficient, achieving a Rabi frequency $f_{\mathrm{Rabi}} \simeq$ 10 MHz with <40 mW (power at the inner loop). This is fast enough for coherent control of the NV electron spin, considering $1/f_{\mathrm{Rabi}} < T_2/10$, where the typical T_2 coherence time for NV electron spins in nanodiamond is around 1 μs [24]. Efficient spin driving with microelectronics is advantageous in use cases where the power budget is limited, such as cryogenic applications, with a view to individual driving of sets of qubit systems. It is worth noting that more efficient driving has been achieved by identifying NVs close to patterned metallization on diamond [25] or nearby wires [26]; however, our demonstration presents a scalable solution using foundry microelectronics, providing both uniformity of the field in the loop to favor NV positioning and compatibility with integrated photonics.

IV. CROSSTALK-MITIGATED SPIN CONTROL

Having demonstrated the ability to efficiently manipulate the spin, we progress to demonstrating the crosstalk-mitigation scheme. By operating both the inner and outer loops [left-hand site in Fig. 2(a)] at the site adjacent to the isolated spin site, our aim is to observe the cancelation of the driving field from this neighboring control site at the position of the isolated spin.

The cancelation condition can be found experimentally by first balancing the effect of the driving fields from the inner and outer loops on the NV spin. The driving field strength can be inferred from continuous-wave optically detected magnetic resonance (ODMR) measurements (see Appendix D). When the microwave source frequency is swept, a dip with a certain depth, the ODMR contrast, is observed at the resonance of the spin-state transition. In the low pump regime (small microwave power) [27], this contrast is proportional to the microwave power. This linearity demonstrates that the ODMR contrast can be directly used to quantify and balance the microwave power measured at the NV site.

Under this crosstalk-mitigation condition, we can now demonstrate coherent spin control. Our scheme considers two adjacent control sites with associated qubits, Q_L and Q_R, as shown in Fig. 4(c). Microwave control for Q_L allows arbitrary single-qubit rotations on the spin two-level system, while independently, Q_R is coherently controlled and evaluated. The crosstalk-mitigated control of Q_R (by canceling the crosstalk field from the other site) means that the control of Q_R will remain coherent, independent of the control signal for Q_L. Otherwise, microwave crosstalk would result in random rotations on Q_L, diminishing the ability to perform coherent qubit control.

For Q_L, the arbitrary rotations $R_{\vec{r}_n}(\phi_n)$ correspond to resonant microwave pulses of different phases, start times, and end times. Randomly chosen rotations can thus be simulated by a resonant microwave signal (at 3.14 GHz) in continuous wave (considering that random pulsing would average out in time) with randomly changing phases. We deliver the same signal to the left-hand inner and outer loops [labeled in Fig. 2(a)] with a π phase shift for the cancelation condition to hold. Note that the cancelation condition holds for arbitrary pulses provided that the relative amplitude and phase remain. Pulse sequences are shown in Fig. 4(d). Rabi sequences (microwave pulses of variable length τ) are then delivered to the right-hand outer loop [similar to Fig. 3(a)].

With the microwave signal in Fig. 4(d) applied, we compare the quantum control of Q_R under different conditions. Figure 4(e) shows the Rabi oscillation performed by the right-hand outer loop alone, serving as a reference. A Rabi frequency of 7 MHz is observed with a fitted decay time $T_2^{\mathrm{Rabi}} = 761 \pm 69$ ns, within which the spin can be coherently driven. In this case, T_2^{Rabi} is an effective timescale set by the applied Rabi pulses, intrinsic spin dephasing, and spin energy relaxation in the host environment, characterizing the controllability of the spin [28,29]. In Fig. 4(f), when the left-hand inner loop is turned on, crosstalk noise is introduced to the Rabi oscillation. The random noise, averaged over the experimental accumulation time, effectively leads to decreased contrast in the Rabi oscillation and thus a reduced T_2^{Rabi} of 249 ± 42 ns. The large decrease in T_2^{Rabi} is expected under strong random driving noise and matches simulations.

Nonetheless, we observe in Fig. 4(g) that when both the left-hand inner and outer loops are on and operated out of phase, the Rabi oscillation is protected, with T_2^{Rabi} tripled to 704 ± 103 ns, meaning that the coherence of the qubit control returns to the level without the neighboring drive field (within the error bars). By numerically simulating the effect of the crosstalk field on the unperturbed Rabi driving [Fig. 4(e)], one can estimate the crosstalk microwave power suppression to be 0.0165 (−35.6 dB, comparing the local Rabi driving power to its induced crosstalk power at the first NN site) from the recovery of the T_2^{Rabi} value. With spin dephasing and crosstalk noise modeled separately, this estimation is not masked by the spin coherence time and is also independently verified through another analytical model (see the Supplemental Material [23]). Note that the −35.6 dB mitigation of the crosstalk field power implies an averaged single-qubit gate infidelity of the order of 10^{-4} [23] and can be further improved by precisely balancing

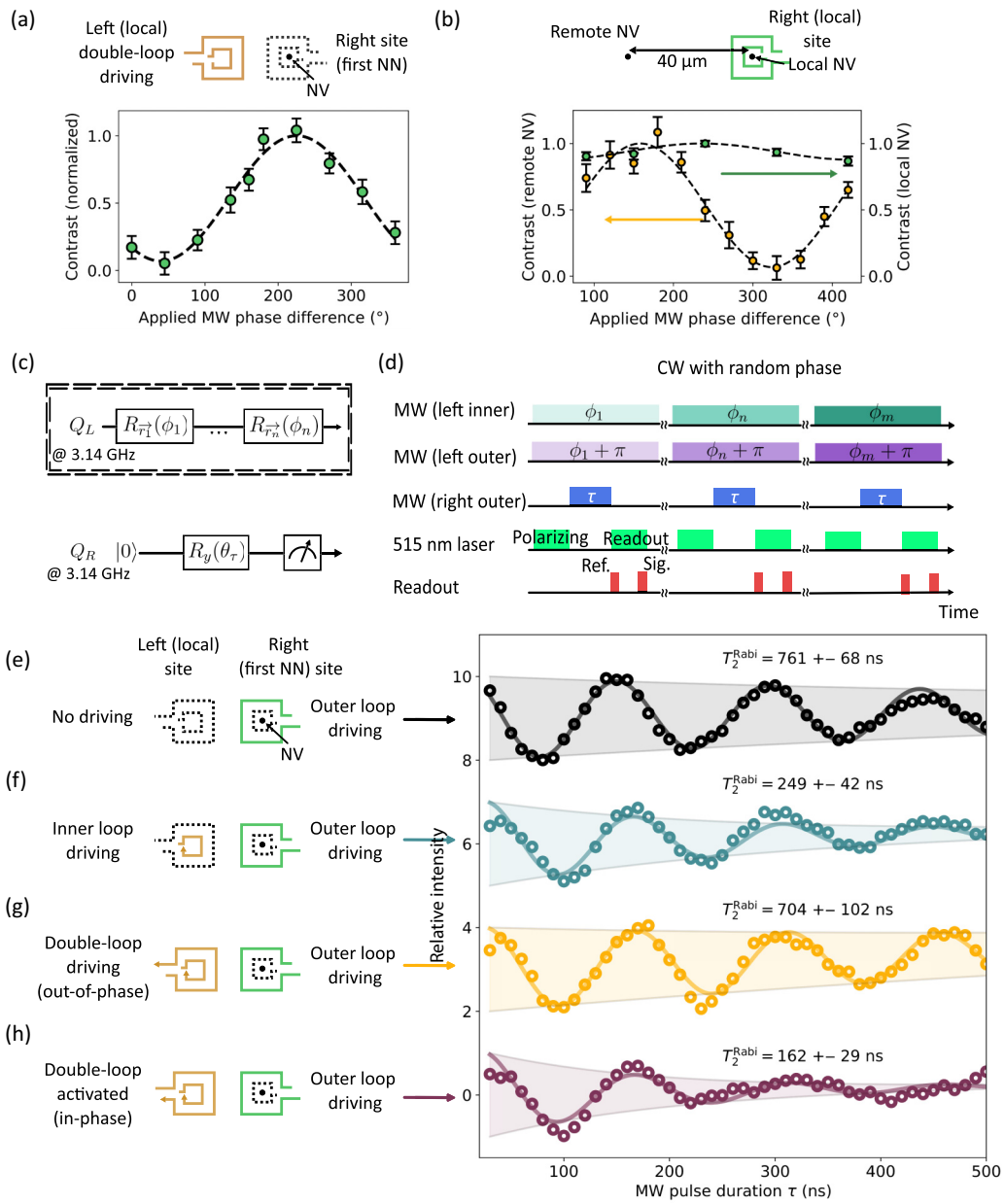

FIG. 4. Active crosstalk canceling. (a) Under the two-loop driving, a sinusoidal relation between the ODMR contrast and the applied phase difference between the two loop feeds is observed. (b) Local NV control is minimally affected under the field-cancelation protocol. Orange data points show results for a remote NV center, and green data points show results for the local NV in the right-hand site. The remote NV 40 µm away is chosen for experimental accessibility. Both the remote and local NV contrast are fitted to a sinusoidal function, and their relative phase shift is due to the difference in NV orientation. The set phase differs from (a) due to differences in experimental conditions. The electron spin resonance is not shifted here to make sure that the spins are driven under the same conditions. (c) Gate sequences for the crosstalk-mitigated spin manipulation, considering two qubits Q_L and Q_R. Random qubit rotations $R_{\vec{r}_n}(\phi_n)$ are performed on Q_L and $R_y(\theta_\tau)$ (rotation around the y axis on the qubit Bloch sphere) performed on Q_R before state readout. There is no detuning between Q_R and Q_L: both qubits operate at 3.14 GHz. (d) Corresponding pulse sequences for demonstrating the crosstalk-mitigated spin manipulation. Microwave pulses in different color shades (top two rows) correspond to different phases. Here, a random phase change occurs every 1 s (while the inner and outer loops are always out of phase), over the >3-h accumulation time for each experiment. The Rabi sequence follows that performed in Fig. 3(a). The microwave power applied to the left-hand loops is larger than that applied to the right-hand loop, allowing a clear observation of spin decoherence under noise. (e) Rabi oscillations driving only the right-hand outer loop. The data are presented with a sinusoidal decay fit and corresponding T_2^{Rabi}. (f) Rabi oscillations with the left-hand inner loop also driving, showing reduced control of the spin qubit. (g) Rabi oscillations protected by the two-loop active cancelation scheme (driving out of phase), showing regained control. (h) Rabi oscillations when the two left-hand loops are in phase, showing increased crosstalk. Note that the Rabi oscillations for (e)–(h) all have the same frequency, around 7 MHz.

the driving of the inner and outer loops to the optimal ratio; this is independent of the original coherence of the system.

In comparison, in Fig. 4(h), when the signals in the left-hand inner and outer loops are in phase, the noise is considerably increased, with $T_2^{\mathrm{Rabi}} = 162 \pm 30$ ns. Note that T_2^{Rabi} here only provides a general indication of spin controllability. The spin coherence, in terms of T_2^*, T_2, and T_1, is also protected to different levels under our crosstalk-mitigation scheme (see simulation results in in the Supplemental Material [23]). Note that T_2^*, T_2, T_1, or more complex randomized benchmarking protocols [30] are not experimentally characterized due to the limited coherence time of the NV centers in nanodiamond used for this proof-of-principle demonstration. For applications where nuclear spins are used for quantum memories [17], the electron-nuclear spin entanglement is also dominated by the electron spin coherence characterized here due to its shorter coherence time.

It is worth noting that we look at the coherence of the same spin with its associated spin environment in the presence of a neighboring qubit and show that it suffers a decrease in coherence when the neighboring qubit is driven, unless the crosstalk-mitigation scheme is used. Our results show that the crosstalk mitigation effectively removes the noise generated by the neighboring control line. Achieving the same level of noise attenuation without this scheme would require a qubit detuning of 40 MHz, where a finite-size frequency band for each qubit imposes architectural complexity, requiring the generation of large gradient fields at scale [31].

V. CONCLUSIONS

We have demonstrated a site-defined control architecture using foundry microelectronics for the scalable manipulation of spin qubits. With NVs lithographically positioned at predefined sites, we showed that their associated electron spins can be driven efficiently, which is important for quantum computing that requires liquid-helium operation to extract coherent photons from NVs and hence has a limited thermal budget. Most importantly, our results demonstrate that crosstalk in driving adjacent spins can be strongly mitigated through an active cancelation scheme without significantly sacrificing this driving efficiency. The scheme works without frequency detuning of spin-qubit transitions [31–33], allowing distinct control of sets of identical qubits. In this work, nanodiamonds are primarily used for ease of prototyping. For large-scale quantum information applications, the use of implanted defect centers in strain-minimized diamond-membrane structures [34] or optically coherent defects in nanophotonic cavities [35,36] would minimize differences in local NV properties, which could also be locally tuned [37].

Figure 5 showcases how the double-loop crosstalk-mitigated microelectronics would fit into existing large-scale quantum information processing hardware for optically active spins [38–40]. The micrometer-scale separation of spin defects in the architecture highlights the need for crosstalk-mitigation microelectronics. Figure 5(a) shows the integration of a 16×16 spin array with input and output photonic links for selective addressing and entangling photonic gates. We consider implanted coherent defect centers such as silicon vacancy (SiV) or tin vacancy (SnV) centers [41] in diamond-membrane chiplets [39,40] to allow coupling to large-scale silicon photonics. Note that crosstalk mitigation becomes even more necessary for highly coherent quantum systems. With a qubit spacing of 15 μm, the double-loop microelectronic control is designed with inner (outer) loop dimensions of 3 μm (6 μm) (see the Supplemental Material [23] for simulation verification), which can be flip-chip bonded [42] to the photonics. The heterogeneous integration schematic is shown in Fig. 5(b). Note that the high-resolution positioning of defect centers, aligned defect orientations in bulk-like diamonds, and negligible inhomogeneity in low-strain material allow (i) a uniform microelectronic design for driving a large-scale system and (ii) the crosstalk-mitigation condition (i.e., drive balancing and phase delay) to be automatically and precisely fulfilled with passive on-chip circuitry, preventing the need for further effort in individual tuning. The calibration complexity of our crosstalk-mitigation method scales as $O(n)$ since it only requires precise positioning of the defect centers. In contrast, the typically used crosstalk-compensation method [43] requires time-consuming pairwise calibration that scales as $O(n^2)$.

For quantum information processing, the photonic resonant transition of defect centers can be tuned electrically [39], which allows single spins along the waveguide to be selected and addressed separately [44]. The tunability also enables multiqubit gates or entanglement of spins across waveguides through interference of emitted photons [45] of the same wavelength. The whole 100-physical-qubit device has a dimension <1 mm^2, demonstrating a high level of integration as demanded for scalable quantum information hardware. For a large-scale spin-driving lattice, we show by simulation that our double-loop driving scheme outperforms single-loop driving, with an additional -35 dB attenuation in the residual crosstalk field [23]. It is also possible to pursue higher densities at smaller process nodes by exploiting the presented crosstalk-cancelation scheme and the significant headroom in the current capacity of the existing circuit. Considering defect-center positioning accuracy with implantation of 50 nm [41] and submicrometer optical modes through confocal microscopy or waveguide mode excitation [46], 1-μm separation should be achievable.

Foundry microelectronics also provides access to mature silicon device libraries to realize static field tuning [47],

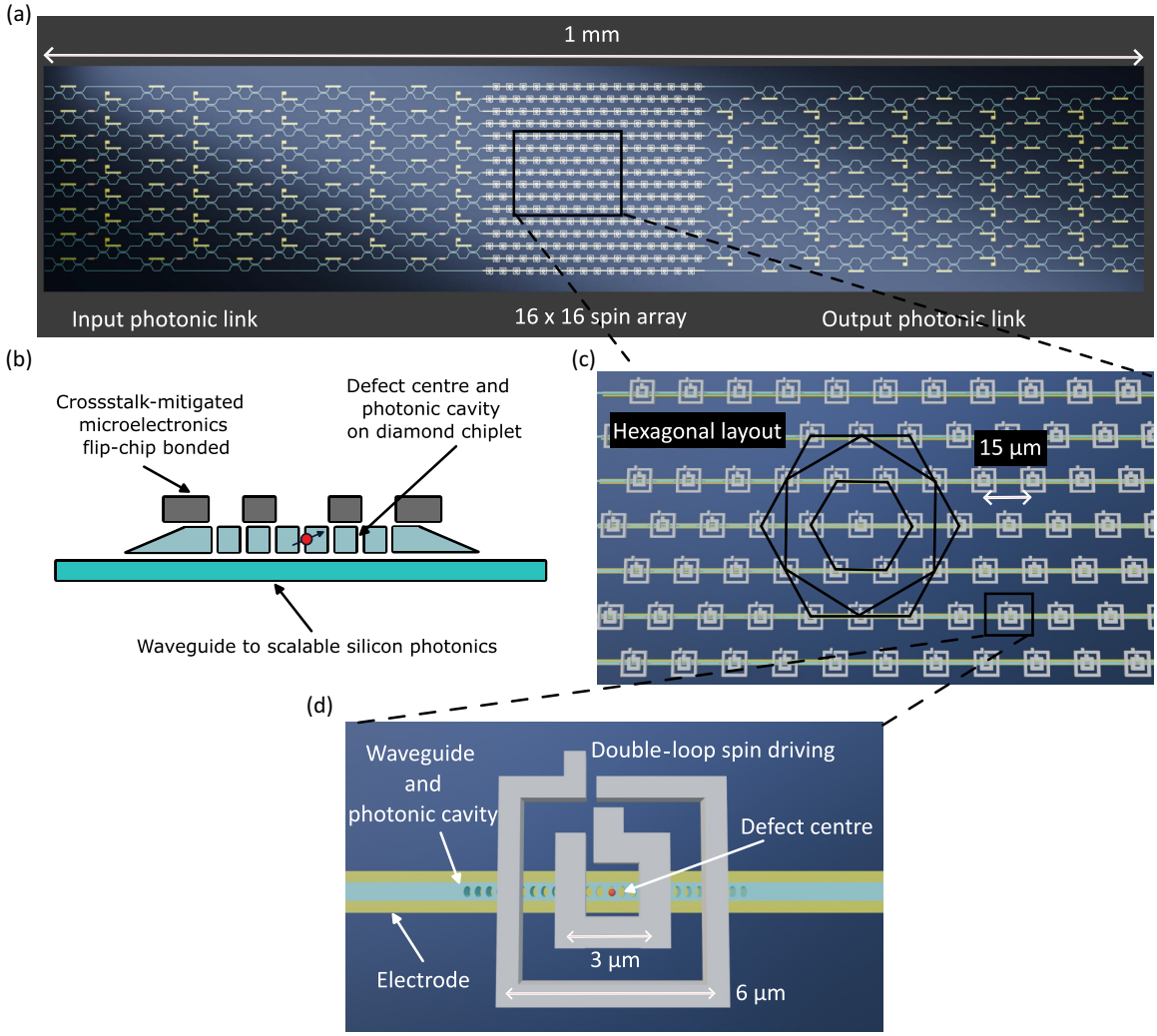

FIG. 5. Schematic device for large-scale quantum information processing: spin qubit integrated with crosstalk-mitigated microelectronics and integrated photonics. (a) Schematic device. The 16 × 16 spin-qubit array is interconnected by photonic links on both sides. The photonics can be used for routing photons and implementing photonic gates that entangle the optically active spins. (b) Heterogeneous combination scheme. Defect centers and photonic cavities are hosted on a membrane diamond chiplet sandwiched by crosstalk-mitigated microelectronics (flip-chip bonded to the top) and scalable photonic integrated circuits (evanescently coupled at the bottom). (c) An enlarged view of the spin-qubit array. The qubits are laid out following the proposed hexagonal architecture in Fig. 1(a) with an interqubit spacing of 15 µm. (d) An enlarged view of a qubit site. The optically active spin qubit is coupled to the photonic cavity on a strip waveguide. The defect-center photonic resonances can be electrically tuned with the yellow electrode under the waveguide. The spin is locally manipulated by the double-loop driving. Here, the inner and outer loops are 3 and 6 µm in diameter, respectively.

electrical spin readout [48,49], photon detection, and logical electronics [20] on the same platform. In combination with photonic integrated circuits, a large-scale spin-photon interfaced quantum information processor could be realized, overcoming space and energy constraints. The scheme presented here is also translatable to alternative quantum platforms that use microwave driving, including other color centers in diamond [50], single spin molecules [51], quantum dots [52], or superconducting circuits [53].

ACKNOWLEDGMENTS

The authors thank J. Monroy-Ruz for building the confocal microscope used in this experiment and S. Komrakova, J. Frazer, and F. Malik for fabrication support. The authors thank J. Monroy-Ruz and J. Matthews for useful discussions. The authors acknowledge funding support from the Quantum Computing and Simulation Hub Partnership Resource Project RFSQ and the Engineering and Physical Sciences Research Council (EPSRC) under Grant No. QC:SCALE EP/W006685/1.

DATA AVAILABILITY

The data that support the findings of this article are openly available [54].

APPENDIX A: ANALYTICAL MODEL EXPRESSION

The analytical model presented (Fig. 1 in the main text) uses the static Biot-Savart approximation. We consider the off-axis field of a current loop centered at the origin in the x-y plane. For any point in space, the magnetic field is defined in a cylindrical coordinate system with the component in the axial direction

$$B_z(r,z) = \gamma\left(E(k)\frac{1-\alpha^2-\beta^2}{(1+\alpha)^2+\beta^2-4\alpha} + K(k)\right) \quad \text{(A1)}$$

and in the radial direction

$$B_r(r,z) = \gamma\left(E(k)\frac{1+\alpha^2+\beta^2}{(1+\alpha)^2+\beta^2-4\alpha} - K(k)\right), \quad \text{(A2)}$$

where $r = \sqrt{x^2+y^2}$ and $\gamma = i\mu_0/2a\pi\sqrt{(1+\alpha)^2+\beta^2}$. Here, μ_0 is the permeability constant, a is the loop radius, i is the current in the loop wire, $K(k)$ is the elliptic integral function of the first kind, $E(k)$ is the elliptic integral function of the second kind, and the constants are defined as $\alpha = r/a$, $\beta = z/a$, $\gamma = z/r$, and $k = \sqrt{4\alpha/(1+\alpha)^2+\beta^2}$.

APPENDIX B: FINITE-ELEMENT SIMULATION DETAILS

To verify the device design, a finite-element model of the structure is carried out in COMSOL MULTIPHYSICS following the analytical model. The double-loop structure is constructed with aluminium metallic loops surrounded by silicon oxide with relative permittivity $\epsilon_r = 4.1$. Lumped ports are defined between the input and output metallic wires of the loops and excited by a voltage source with the port phase set in simulation. The Electromagnetic Wave, Frequency Domain analysis COMSOL package is used to study the device at 2.87 GHz. The minor differences between the analytical and simulation results are due to the physical width of the wires of the loop structure, which is not considered in the analytical model.

APPENDIX C: DEVICE FABRICATION DETAILS

We employ the 0.13 μm IHP-SG13G2 BiCMOS technology with two thick metal layers for current-carrying applications and five thin metal layers for interconnections. The track widths of the inner (outer) loops are 5.5 μm (4 μm), both on the same 2-μm-thick aluminium layer.

For nanodiamond positioning (following [55]), nanodiamonds are sized around 50 nm in diameter, milled from high-pressure high-temperature diamond (Nabond). First, a postprocess inductively coupled plasma etch is used to release the inner region of the device, creating a 5-μm-deep trench. This allows nanodiamonds to be positioned at the centers of the loops. A layer of polymethyl methacrylate (PMMA) is then coated and patterned by electron-beam lithography (Raith Voyager). This creates sites on the PMMA mask on which the nanodiamond (suspended in methanol) is dropcast. Removing the PMMA then results in nanodiamonds positioned precisely on the predefined sites.

APPENDIX D: EXPERIMENTAL SETUP

A scanning confocal microscope is used to optically address the NVs in this work. With a 0.9-numerical-aperture (NA) microscope objective (Olympus M Plan N 100 × /0.90NA), the excitation beam (515 nm, Cobolt 06-MLD) is focused on the sample to a nearly diffraction-limited spot (<1 μm diameter). The NV photoluminescence is collected through the same lens and separated from the excitation path using a dichroic mirror. By using a high-NA objective, the NV PL is efficiently extracted from background fluorescence, such as scattering from metal layers. Electronically, for the demonstration of active cancelation, the microwave source (Rohde & Schwarz SMB100AP20) is split by a power splitter (Mini-Circuits ZN2PD2-63-S+) to drive the inner and outer right-hand metallic-loop interfaces. On one path, an additional tunable power attenuator (Mini-Circuits RCDAT-6G-120H) and phase shifter (Vaunix LPS-802) are applied. Both paths are amplified (Microwave Amplifiers Ltd. AM4-2-6-43-43R) and fed to an isolator (DiTom Microwave D3C2040) before the device-under-test. Time tagging and pulsing are recorded by UQDevices Logic-16 and Swabian Instruments Pulse Streamer 8/2. The electronic setup for crosstalk-mitigated spin control differs only by an additional random phase shifter applied before power splitting. Pulsing is achieved using a microwave switch (Mini-Circuits, ZASW-2-50DR+, DC-5 GHz) in Rabi-oscillation measurements.

We perform electron spin-Rabi oscillations by driving the NV ground-state triplets ($|0\rangle_e$ and $|\pm 1\rangle_e$). Figure 3(a) shows the corresponding pulse sequences. The electron spin is first polarized into the $|0\rangle_e$ state by a 3-μs-long 515-nm laser pulse. A microwave pulse of length τ is then applied to resonantly drive the transition $|0\rangle_e \longleftrightarrow |+1\rangle_e$ (with the ground-state zero-field splitting around 2.87 GHz). In our measurement, an external static magnetic field is applied using a strong permanent magnet to lift the degeneracy of the two transitions ($|0\rangle_e \longleftrightarrow |+1\rangle_e$ and $|0\rangle_e \longleftrightarrow |-1\rangle_e$) and to shift the resonances to best match the on-chip loop resonance. Another laser pulse of 3 μs is used to read out the spin state by the PL intensity (stronger in the $|0\rangle_e$ state and weaker in the $|\pm 1\rangle_e$

state due to state-dependent intersystem crossing). The PL intensity is extracted by summing the photon count in the first 0.5 μs interval and normalizing to the count summed over the last 1.5 μs. We use the same laser pulse to polarize and read out the electron state. In Figs. 3(b)–3(g), the Rabi measurements are presented (in the y axis) with the relative intensity normalized between ± 1 for comparison. For the Rabi-oscillation results presented in Figs. 4(e)–4(h), the error in decay time is deduced from the variance of the parameter estimation during fitting, representing one standard deviation. The slight drift in oscillation is an artifact due to device heating under microwave power.

In the continuous-wave (CW) ODMR measurements, the 515-nm laser is kept constantly on while the frequency of the microwave source is swept around the resonance of the electron-spin transitions. Due to the difference in PL intensity for the electron states, a dip is observed at the resonances with a certain depth (the ODMR contrast). The contrast is extracted by fitting the measured PL intensity across frequency sweeps to a Gaussian dip. Error bars, showing one standard deviation in photon counts, arise from photon shot noise and low drift of the experimental setup.

The field-cancelation extinction ratio (directly proportional to the residual crosstalk field) is undetectable (within experimental error bars) from the CW-ODMR measurements [Figs. 4(a)–4(b)] and Rabi-oscillation lifetimes [Figs. 4(e)–4(h)] directly. Fitting the results to a numerical model, a -15 dB extinction ratio is estimated, inferring an additional -15 dB crosstalk power attenuation when comparing the single-loop driving and the double-loop driving. For our case demonstrated in Figs. 4(e)–4(h), a -20 dB imbalance of microwave power (from the left-hand loops) at the NV reduces T_2^{Rabi} by only 2% under active-cancelation protection, and a -30 dB imbalance reduces it by 0.2%.

[1] F. Arute, K. Arya, R. Babbush, D. Bacon, J. C. Bardin, R. Barends, R. Biswas, S. Boixo, F. G. Brandao, D. A. Buell *et al.*, Quantum supremacy using a programmable superconducting processor, Nature **574**, 505 (2019).

[2] H.-S. Zhong, H. Wang, Y.-H. Deng, M.-C. Chen, L.-C. Peng, Y.-H. Luo, J. Qin, D. Wu, X. Ding, Y. Hu *et al.*, Quantum computational advantage using photons, Science **370**, 1460 (2020).

[3] S. J. Evered, D. Bluvstein, M. Kalinowski, S. Ebadi, T. Manovitz, H. Zhou, S. H. Li, A. A. Geim, T. T. Wang, N. Maskara *et al.*, High-fidelity parallel entangling gates on a neutral-atom quantum computer, Nature **622**, 268 (2023).

[4] M. Kjaergaard, M. E. Schwartz, J. Braumüller, P. Krantz, J. I.-J. Wang, S. Gustavsson, and W. D. Oliver, Superconducting qubits: Current state of play, Annu. Rev. Condens. Matter Phys. **11**, 369 (2020).

[5] A. G. Fowler, M. Mariantoni, J. M. Martinis, and A. N. Cleland, Surface codes: Towards practical large-scale quantum computation, Phys. Rev. A **86**, 032324 (2012).

[6] J. Gambetta, IBM's roadmap for scaling quantum technology, IBM Research Blog (September 2020) (2020).

[7] S. Bravyi, O. Dial, J. M. Gambetta, D. Gil, and Z. Nazario, The future of quantum computing with superconducting qubits, J. Appl. Phys. **132**, 160902 (2022).

[8] G. Kurizki, P. Bertet, Y. Kubo, K. Mølmer, D. Petrosyan, P. Rabl, and J. Schmiedmayer, Quantum technologies with hybrid systems, Proc. Natl. Acad. Sci. **112**, 3866 (2015).

[9] D. Ristè, S. Fallek, B. Donovan, and T. A. Ohki, Microwave techniques for quantum computers: State-of-the-art control systems for quantum processors, IEEE. Microw. Mag. **21**, 60 (2020).

[10] J. C. Bardin, D. H. Slichter, and D. J. Reilly, Microwaves in quantum computing, IEEE J. Microwaves **1**, 403 (2021).

[11] T. Brecht, W. Pfaff, C. Wang, Y. Chu, L. Frunzio, M. H. Devoret, and R. J. Schoelkopf, Multilayer microwave integrated quantum circuits for scalable quantum computing, npj Quantum Inf. **2**, 1 (2016).

[12] B. Lekitsch, S. Weidt, A. G. Fowler, K. Mølmer, S. J. Devitt, C. Wunderlich, and W. K. Hensinger, Blueprint for a microwave trapped ion quantum computer, Sci. Adv. **3**, e1601540 (2017).

[13] P. A. Spring, S. Cao, T. Tsunoda, G. Campanaro, S. Fasciati, J. Wills, M. Bakr, V. Chidambaram, B. Shteynas, L. Carpenter *et al.*, High coherence and low cross-talk in a tileable 3D integrated superconducting circuit architecture, Sci. Adv. **8**, eabl6698 (2022).

[14] C. Piltz, T. Sriarunothai, A. F. Varón, and C. Wunderlich, A trapped-ion-based quantum byte with 10^{-5} next-neighbour cross-talk, Nat. Commun. **5**, 4679 (2014).

[15] H. Wang, M. E. Trusheim, L. Kim, H. Raniwala, and D. R. Englund, Field programmable spin arrays for scalable quantum repeaters, Nat. Commun. **14**, 704 (2023).

[16] G. Clark, H. Raniwala, M. Koppa, K. Chen, A. Leenheer, M. Zimmermann, M. Dong, L. Li, Y. H. Wen, D. Dominguez *et al.*, Nanoelectromechanical control of spin–photon interfaces in a hybrid quantum system on chip, Nano Lett. **24**, 1316 (2024).

[17] M. Pompili, S. L. N. Hermans, S. Baier, H. K. Beukers, P. C. Humphreys, R. N. Schouten, R. F. L. Vermeulen, M. J. Tiggelman, L. dos Santos Martins, B. Dirkse *et al.*, Realization of a multinode quantum network of remote solid-state qubits, Science **372**, 259 (2021).

[18] M. H. Abobeih, Y. Wang, J. Randall, S. J. Loenen, C. E. Bradley, M. Markham, D. J. Twitchen, B. M. Terhal, and T. H. Taminiau, Fault-tolerant operation of a logical qubit in a diamond quantum processor, Nature **606**, 884 (2022).

[19] K. Bian, W. Zheng, X. Zeng, X. Chen, R. Stöhr, A. Denisenko, S. Yang, J. Wrachtrup, and Y. Jiang, Nanoscale electric-field imaging based on a quantum sensor and its charge-state control under ambient condition, Nat. Commun. **12**, 2457 (2021).

[20] D. Kim, M. I. Ibrahim, C. Foy, M. E. Trusheim, R. Han, and D. R. Englund, A CMOS-integrated quantum sensor based on nitrogen–vacancy centers, Nat. Electron. **2**, 284 (2019).

[21] X. Yang, N. Zhang, H. Yuan, G. Bian, P. Fan, and M. Li, Microstrip-line resonator with broadband, circularly polarized, uniform microwave field for nitrogen vacancy center ensembles in diamond, AIP Adv. **9**, 075213 (2019).

[22] K. Fujimoto and H. Morishita, *Modern Small Antennas* (Cambridge University Press, Cambridge, 2014).

[23] See Supplemental Material at http://link.aps.org/supplemental/10.1103/stgn-ysxr for additional experimental results, characterizations, and simulations. The Supplemental Material also includes Refs. [56–61].

[24] H. S. Knowles, D. M. Kara, and M. Atatüre, Observing bulk diamond spin coherence in high-purity nanodiamonds, Nat. Mater. **13**, 21 (2014).

[25] G. Mariani, S. Nomoto, S. Kashiwaya, and S. Nomura, System for the remote control and imaging of MW fields for spin manipulation in NV centers in diamond, Sci. Rep. **10**, 4813 (2020).

[26] P. Wang, Z. Yuan, P. Huang, X. Rong, M. Wang, X. Xu, C. Duan, C. Ju, F. Shi, and J. Du, High-resolution vector microwave magnetometry based on solid-state spins in diamond, Nat. Commun. **6**, 6631 (2015).

[27] A. Dréau, M. Lesik, L. Rondin, P. Spinicelli, O. Arcizet, J.-F. Roch, and V. Jacques, Avoiding power broadening in optically detected magnetic resonance of single NV defects for enhanced dc magnetic field sensitivity, Phys. Rev. B **84**, 195204 (2011).

[28] R. Hanson, O. Gywat, and D. D. Awschalom, Room-temperature manipulation and decoherence of a single spin in diamond, Phys. Rev. B **74**, 161203(R) (2006).

[29] L. M. K. Vandersypen and I. L. Chuang, NMR techniques for quantum control and computation, Rev. Mod. Phys. **76**, 1037 (2005).

[30] H. P. Bartling, J. Yun, K. N. Schymik, M. van Riggelen, L. A. Enthoven, H. B. van Ommen, M. Babaie, F. Sebastiano, M. Markham, D. Twitchen *et al.*, Universal high-fidelity quantum gates for spin qubits in diamond, Phys. Rev. Appl. **23**, 034052 (2025).

[31] I. Jakobi, P. Neumann, Y. Wang, D. B. R. Dasari, F. El Hallak, M. A. Bashir, M. Markham, A. Edmonds, D. Twitchen, and J. Wrachtrup, Measuring broadband magnetic fields on the nanoscale using a hybrid quantum register, Nat. Nanotechnol. **12**, 67 (2017).

[32] P. Neumann, R. Kolesov, B. Naydenov, J. Beck, F. Rempp, M. Steiner, V. Jacques, G. Balasubramanian, M. L. Markham, D. J. Twitchen *et al.*, Quantum register based on coupled electron spins in a room-temperature solid, Nat. Phys. **6**, 249 (2010).

[33] Y. Sekiguchi, K. Matsushita, Y. Kawasaki, and H. Kosaka, Optically addressable universal holonomic quantum gates on diamond spins, Nat. Photonics **16**, 662 (2022).

[34] X. Guo, M. Xie, A. Addhya, A. Linder, U. Zvi, S. Wang, X. Yu, T. D. Deshmukh, Y. Liu, I. N. Hammock *et al.*, Direct-bonded diamond membranes for heterogeneous quantum and electronic technologies, Nat. Commun. **15**, 8788 (2024).

[35] L. Orphal-Kobin, K. Unterguggenberger, T. Pregnolato, N. Kemf, M. Matalla, R.-S. Unger, I. Ostermay, G. Pieplow, and T. Schröder, Optically coherent nitrogen-vacancy defect centers in diamond nanostructures, Phys. Rev. X **13**, 011042 (2023).

[36] A. Gokhale, J. M. Bopp, L. Orphal-Kobin, K. Unterguggenberger, M. E. Stucki, T. Pregnolato, and T. Schröder, in *European Quantum Electronics Conference* (Optica Publishing Group, Munich, 2025), p. eb_5_2.

[37] F. Dolde, H. Fedder, M. W. Doherty, T. Nöbauer, F. Rempp, G. Balasubramanian, T. Wolf, F. Reinhard, L. C. L. Hollenberg, F. Jelezko *et al.*, Electric-field sensing using single diamond spins, Nat. Phys. **7**, 459 (2011).

[38] S. Simmons, Scalable fault-tolerant quantum technologies with silicon color centers, PRX Quantum **5**, 010102 (2024).

[39] L. Li, L. D. Santis, I. B. W. Harris, K. C. Chen, Y. Gao, I. Christen, H. Choi, M. Trusheim, Y. Song, C. Errando-Herranz *et al.*, Heterogeneous integration of spin–photon interfaces with a CMOS platform, Nature **630**, 70 (2024).

[40] N. H. Wan, T.-J. Lu, K. C. Chen, M. P. Walsh, M. E. Trusheim, L. De Santis, E. A. Bersin, I. B. Harris, S. L. Mouradian, I. R. Christen *et al.*, Large-scale integration of artificial atoms in hybrid photonic circuits, Nature **583**, 226 (2020).

[41] X. Cheng, A. Thurn, G. Chen, G. S. Jones, J. E. Bennett, M. Coke, M. Adshead, C. P. Michaels, O. Balci, A. C. Ferrari *et al.*, Laser activation of single group-IV color centers in diamond, Nat. Commun. **16**, 5124 (2025).

[42] S. Daudlin, A. Rizzo, S. Lee, D. Khilwani, C. Ou, S. Wang, A. Novick, V. Gopal, M. Cullen, R. Parsons *et al.*, Three-dimensional photonic integration for ultra-low-energy, high-bandwidth interchip data links, Nature Photonics **19**, 502 (2025).

[43] R. Acharya, D. A. Abanin, L. Aghababaie-Beni, I. Aleiner, T. I. Andersen, M. Ansmann, F. Arute, K. Arya, A. Asfaw, N. Astrakhantsev *et al.*, Quantum error correction below the surface code threshold, Nature **626**, 705 (2024).

[44] L. Robledo, L. Childress, H. Bernien, B. Hensen, P. F. A. Alkemade, and R. Hanson, High-fidelity projective readout of a solid-state spin quantum register, Nature **477**, 574 (2011).

[45] H. K. C. Beukers, M. Pasini, H. Choi, D. Englund, R. Hanson, and J. Borregaard, Remote-entanglement protocols for stationary qubits with photonic interfaces, PRX Quantum **5**, 010202 (2024).

[46] M. K. Bhaskar, D. D. Sukachev, A. Sipahigil, R. E. Evans, M. J. Burek, C. T. Nguyen, L. J. Rogers, P. Siyushev, M. H. Metsch, H. Park *et al.*, Quantum nonlinear optics with a germanium-vacancy color center in a nanoscale diamond waveguide, Phys. Rev. Lett. **118**, 223603 (2017).

[47] K. Arai, C. Belthangady, H. Zhang, N. Bar-Gill, S. J. DeVience, P. Cappellaro, A. Yacoby, and R. L. Walsworth, Fourier magnetic imaging with nanoscale resolution and compressed sensing speed-up using electronic spins in diamond, Nat. Nanotechnol. **10**, 859 (2015).

[48] E. Bourgeois, A. Jarmola, P. Siyushev, M. Gulka, J. Hruby, F. Jelezko, D. Budker, and M. Nesladek, Photoelectric detection of electron spin resonance of nitrogen-vacancy centers in diamond, Nat. Commun. **6**, 8577 (2015).

[49] M. Gulka, D. Wirtitsch, V. Ivády, J. Vodnik, J. Hruby, G. Magchiels, E. Bourgeois, A. Gali, M. Trupke, and M. Nesladek, Room-temperature control and electrical readout of individual nitrogen-vacancy nuclear spins, Nat. Commun. **12**, 4421 (2021).

[50] S. Castelletto and A. Boretti, Silicon carbide color centers for quantum applications, J. Phys.: Photonics **2**, 022001 (2020).

[51] A. Gaita-Ariño, F. Luis, S. Hill, and E. Coronado, Molecular spins for quantum computation, Nat. Chem. **11**, 301 (2019).

[52] W. I. L. Lawrie, M. Rimbach-Russ, F. van Riggelen, N. W. Hendrickx, S. L. de Snoo, A. Sammak, G. Scappucci, J. Helsen, and M. Veldhorst, Simultaneous single-qubit driving of semiconductor spin qubits at the fault-tolerant threshold, Nat. Commun. **14**, 3617 (2023).

[53] B. K. Mitchell, R. K. Naik, A. Morvan, A. Hashim, J. M. Kreikebaum, B. Marinelli, W. Lavrijsen, K. Nowrouzi, D. I. Santiago, and I. Siddiqi, Hardware-efficient microwave-activated tunable coupling between superconducting qubits, Phys. Rev. Lett. **127**, 200502 (2021).

[54] H.-C. Weng, Data availability for crosstalk-mitigated microelectronic control for optically-active spins arXiv:2404.04075, 2026, https://doi.org/10.5281/zenodo.18157704.

[55] H.-C. Weng, J. Monroy-Ruz, J. C. F. Matthews, J. G. Rarity, K. C. Balram, and J. A. Smith, Heterogeneous integration of solid-state quantum systems with a foundry photonics platform, ACS Photonics **10**, 3302 (2023).

[56] J. B. Hagen, *Radio-Frequency Electronics: Circuits and Applications* (Cambridge University Press, UK, 2009).

[57] D. V. Vertyanov, I. A. Belyakov, S. P. Timoshenkov, A. V. Borisova, and V. N. Sidorenko, in *2020 IEEE Conference of Russian Young Researchers in Electrical and Electronic Engineering (EIConRus)* (IEEE, Moscow, 2020), pp. 2216–2220.

[58] M. Iannuzzi, Bias humidity performance and failure mechanisms of nonhermetic aluminum SIC's in an environment contaminated with Cl_2, IEEE Trans. Compon. Hybrid Manuf. Technol. **6**, 191 (1983).

[59] J. R. Johansson, P. D. Nation, and F. Nori, QuTiP: An open-source Python framework for the dynamics of open quantum systems, Comput. Phys. Commun. **183**, 1760 (2012).

[60] S. Wimperis, Broadband, narrowband, and passband composite pulses for use in advanced NMR experiments, J. Magn. Reson., Ser. A **109**, 221 (1994).

[61] Z. Yuan, S. Mukherjee, J. D. Thompson, N. P. de Leon, A. Gardill, and S. Kolkowitz, An instructional lab apparatus for quantum experiments with single nitrogen-vacancy centers in diamond, Am. J. Phys. **92**, 892 (2024).